

Comparison of FASTMAP and B_0 Field Map Shimming at 4T: Magnetic Field Mapping Using a Gradient-Echo Pulse Sequence

Mohan Jayatilake^{1,2}, Christopher T. Sica¹, Rommy Elyan¹, Prasanna Karunanayaka^{1,2*}

¹Department of Radiology (Center for NMR Research), Pennsylvania State University College of Medicine, Milton S. Hershey Medical Center, Hershey, Pennsylvania, USA

²Department of Physics, University of Cincinnati, Cincinnati, Ohio, USA

Email: jayatilake@gmail.com, csica@pennstatehealth.psu.edu, relyan@pennstatehealth.psu.edu,

*pkarunanayaka@pennstatehealth.psu.edu

How to cite this paper: Jayatilake, M., Sica, C.T., Elyan, R. and Karunanayaka, P. (2020) Comparison of FASTMAP and B_0 Field Map Shimming at 4T: Magnetic Field Mapping Using a Gradient-Echo Pulse Sequence. *Journal of Electromagnetic Analysis and Applications*, 12, 115-130.

<https://doi.org/10.4236/jemaa.2020.128010>

Received: June 29, 2020

Accepted: August 28, 2020

Published: August 31, 2020

Copyright © 2020 by author(s) and Scientific Research Publishing Inc. This work is licensed under the Creative Commons Attribution International License (CC BY 4.0).

<http://creativecommons.org/licenses/by/4.0/>



Open Access

Abstract

Local susceptibility variations result in B_0 field inhomogeneities, causing distortions and signal losses in MR imaging. Susceptibility variations become stronger with increasing B_0 magnetic field strength. Active shimming is used to generate corrective magnetic fields, which can be used to improve B_0 field homogeneity. FASTMAP is an effective shimming technique for computing optimal coil currents, which uses data from six projection directions (or columns): this technique is routinely used for shimming cubic volumes of interest (VOIs). In this paper, we propose several improvements to FASTMAP at 4T. For each shim coil, using a modified 3D gradient-echo pulse sequence, we compute B_0 inhomogeneity maps and project them onto eight 1st and 2nd order spherical harmonic functions. This process is repeated for shim currents between $-15,000$ to $15,000$ with increments of 5000 Digital to Analog Converter (DAC) units, and is used to compute the gradient between spherical harmonic coefficients and DAC values for all 8 shim coils—along with the R^2 values of linear fits. A method is proposed (based on R^2 values) to further refine optimal shim currents in respective coils. We present an analysis that is numerically robust and completely flexible in the selection of the VOIs for shimming. Performance analyses, phantom results, and *in vivo* results of a human brain are presented, comparing our methods with the FASTMAP method.

Keywords

MRI, Shimming, 4T, Higher-Order Shims

1. Introduction

Automatic shimming for optimizing magnetic field uniformities is highly desirable in MR spectroscopy. Objects are often heterogeneous and contain intrinsically unshimmable field variations due to rapid susceptibility changes, which can lead to distortions of the lineshape obtained from the volume [1] [2] [3]. Several shimming techniques using volumes of interest (VOIs) have been proposed in order to improve the B_0 field homogeneity [3]-[8]. For example, Holtz *et al.* (1988) used a surface coil [3] and the signal integral of the free induction decay (FID) over a VOI, iteratively, for field optimization [7]-[12]; however, this technique is time-consuming and impractical for many *in vivo* applications. Moreover, the FID (or the spectral peak amplitudes) is sensitive to changes in shim settings [7] [9] [10] [11] [12] [13].

The use of linear shim coils is highly advantageous in MR imaging [10] [11]. The use of second, or higher-order, shim coils can introduce nonlinear interactions in the B_0 field; specifically, whenever the origin of the VOI is offset from the isocenter [9] [10] [11] [12]. The fast automatic shimming technique, by mapping along projections (FASTMAP) [13] [14] [15], has been very effective in improving B_0 field inhomogeneity [5] [16] [17] [18] [19]. This method computes the corrective first and second-order shim currents by mapping the B_0 field along six projection directions (or columns). FASTMAP, however, is restricted to selected cubic VOIs [5] [18] [20] [21] [22].

FASTMAP works well over reasonably homogeneous volumes with moderate field inhomogeneity [20] [23]. This technique performs well in applications probing smaller volumes (e.g., single voxel spectroscopy) [24], but not larger ones. For example: during human brain imaging studies at high-fields where VOIs are extended into the frontal and inferior brain regions; where off-resonance may be present, or whenever fields rapidly change.

The FASTMAP technique incorrectly assumes that shim coil fields can be fully characterized by a minimal set of spherical harmonics [25] [26]. Therefore, a shimming technique less susceptible to signal voids than projection based methods, and capable of handling arbitrarily shaped VOIs is highly desirable.

In this paper, we follow the same general principals outlined in FASTMAP but propose several improvements. In brief, we propose combining spherical harmonic functions and linear least squares fitting for estimating field inhomogeneity. This method entails the computation of 3D phase images and the determination of first and second-order spherical harmonic coefficients for specific shim currents, by changing the Digital to Analog Converter (DAC) settings, which control voltages across different shim coils. The spherical harmonic calibration constants are then determined by computing the gradients between spherical harmonic coefficients and the DAC values of each coil—followed by a first order correction [see Equation (5)]. Our analysis is numerically robust and completely flexible when selecting VOIs for shimming. A performance analysis comparing our technique with FASTMAP, on a phantom and a human brain, demonstrates

how our proposed method outperforms the FASTMAP technique in terms of B_0 homogeneity.

2. Methods

2.1. Equipment

All experiments were performed on a 4T whole-body Varian INOVA (Palo Alto, CA) MRI scanner located in Cincinnati, Ohio. The system was equipped with the following resistive shim coils: X, Z, Y ($n = 1, m = 1, 0, -1$) and second-order [$X^2 - Y^2, ZX, Z^2, ZY, XY$ ($n = 2, m = -2, -1, 0, 1, 2$)]. A TEM volume head coil was used for RF transmission and reception.

2.2. Imaging

The imaging protocol employed a modified 3D gradient-echo pulse sequence (see **Figure S1** in supplementary material), which was used to obtain B_0 field maps. Frequency distortion correction (along the read-out direction) was performed on B_0 field maps. All acquisitions used a $256 \times 256 \times 256$ mm field of view; a $128 \times 64 \times 64$ acquisition matrix; a 10° pulse flip angle; a repetition time (TR) of 16 ms, and echo times of 5.25 ms and 7 ms. The data was acquired in the axial orientation, with a slab-selective pulse used for excitation.

After acquisition, inverse Fourier transformation was performed on the acquired 3D k-space data. Subsequently, 3D phase unwrapping was performed on the resultant phase images as necessary. Frequency maps were then computed from the difference of the two phase images (acquired at different echo times) with the following equation:

$$f(x, z, y) = \frac{\gamma \cdot \Delta B_0(x, y, z)}{2\pi} \quad (1)$$

After calculation of the 3D frequency maps, voxels corresponding to the selected VOI were extracted. All image reconstruction steps were performed in Matlab (Mathworks, Natick, MA).

Images were obtained in both a phantom and *in-vivo*. The phantom was a water sphere with a diameter of 178 mm. *In-vivo* images of a human head were obtained from a single subject. Consent was obtained with an IRB protocol approved by the University of Cincinnati School of Medicine. The VOI for shimming was defined as the entire spherical phantom and the brain only, respectively (see supplementary material for details). B_0 field maps were acquired both prior to, and after, the shimming procedure outlined below.

2.3. Constructing Calibration Tables for Active Shimming

A one-time procedure was performed to construct shim calibration tables for active shimming. B_0 field maps were acquired upon each of the system's 8 shim coils at different shim current levels. Specifically, the shim current was varied from $-15,000$ to $15,000$ by increments of 5000 per acquisition. Thus, 7 field maps were acquired per shim coil. A spherical phantom ($d = 178$ mm) was used

as the reference object for this calibration procedure. After reconstruction of the 3D phase images for each shim coil, and shim current setting, frequency distribution maps were computed. The matrix representation of $f(x, y, z)$ is given by:

$$f(x, y, z) = \sum_{n=0}^{\infty} \sum_{m=0}^n F_{n,m}(x_i, y_j, z_k) \cdot \eta_{nm} \quad (2)$$

where η_{nm} are the coefficients of spherical harmonics, and $F_{n,m}$ is the Cartesian spherical harmonic spatial dependence function (see **Figure S4**). Using the linear least-squares method, the optimized spherical harmonic coefficients of the first- and second-order shim coils over the selected VOI can be estimated. The frequency distributions of all shim coils (at each DAC step) can be projected onto the spherical harmonics by using Equation (2). We assume that the $\eta_{nm,g,l}$ of each shim coil is linearly varying with the DAC values.

$$\eta_{nm,g,l} = C_{nm,g} \cdot DAC_{l,g} \quad (3)$$

Here, $C_{nm,g}$ is the calibration constant for each spherical harmonic. These $C_{nm,g}$ values can be estimated using the following expression:

$$C_{nm,g} = \left(\left(DAC_{l,g}^T \cdot DAC_{l,g} \right)^{-1} \cdot DAC_{l,g} \cdot \eta_{nm,g,l}^T \right)^T \quad (4)$$

The $C_{nm,g}$ values for all 8 shim coils are obtained from **Figures S4-S6**. Finally, the spherical harmonic calibration constants are computed by the gradient between spherical harmonic coefficients and the DAC values of each coil; this can be used to update the DAC settings. The R^2 of this linear fit was also computed (see supplementary material for details).

2.4. Correction Procedure for 1st Order Shims

Generally, first order coils should produce orthogonal fields that correspond to first order spherical harmonics. The second order coils could potentially produce fields that correspond to first and second-order spherical harmonics. Therefore, we propose the following correction when computing optimal DAC settings of first-order shims, in order to counter the contributions of second-order shims:

$$DAC_{1,m_1} \Big|_{Corrected} = DAC_{1,m_1} - \frac{C_{2,m_2} \times DAC_{2,m_2}}{C_{1,m_1}} \quad (5)$$

Here, DAC_{1,m_1} is the shim setting of the 1st order m_1^{th} degree coil (X , Y , or Z), and DAC_{1,m_1} is the setting for the 2nd order m_2^{th} degree shim coil for correct shimming of an object. C_{1,m_1} and C_{2,m_2} are the 1st order m_1^{th} degree, and the 2nd order m_2^{th} degree calibration coefficients of coils, respectively. The term $C_{2,m_2} \times DAC_{2,m_2}$ is the contribution of the second-order coil to the first-order spherical harmonics. Multiplying the term $C_{2,m_2} \times DAC_{2,m_2}$ by a proportionality constant $\frac{1}{C_{1,m_1}}$, then using Equation (4), we can compute an updated DAC_{1,m_1}

setting. This new setting has effectively subtracted the contributions of the second order coil from the first order coil (or first order spherical harmonics).

3. Results

Spherical harmonic calibration constants and corresponding R^2 values of linear fits (for all shims) are tabulated in **Table 1** and **Table 2**, which are used to compute optimal DAC settings for shimming an object. Second-order shims seem to exhibit higher R^2 values in spherical harmonic calibration constants for first-order shims (**Table 2**). R^2 values that are ≥ 0.9 are highlighted in light blue in **Table 2**. For example, changes in DAC values of the xy coil influence coefficients of some

Table 1. Spherical harmonic calibration constants. Spherical harmonic coefficients corresponding to frequency distribution maps of objects are multiplied by calibration constants to obtain DAC settings for optimal shimming.

Coefficient	Notation	Spherical Harmonic Calibration Constant (Cnm > g)							
		X-Coil	Z-Coil	Y-Coil	X ² Y ² -Coil	XZ-Coil	Z ² C-Coil	ZY-Coil	XY-Coil
A_{11}	X	-2.3E-03	-2.7E-07	-8.0E-07	-5.0E-05	1.3E-05	2.6E-05	2.1E-05	-1.4E-05
A_{10}	Z	-6.2E-07	2.3E-03	2.3E-06	1.7E-04	-2.2E-05	4.6E-05	-7.0E-06	-2.1E-04
$A_{1,-1}$	Y	-1.1E-06	-1.6E-06	-2.3E-03	3.1E-06	2.2E-05	-1.2E-05	-2.0E-05	2.9E-05
A_{22}	$X^2 - Y^2$	3.9E-07	-1.0E-07	-1.8E-07	-2.1E-04	-1.6E-07	-3.9E-07	1.7E-07	3.8E-06
A_{21}	ZX	-8.0E-07	-3.6E-07	-5.9E-08	-6.3E-06	-1.8E-04	4E-07	2.4E-07	5.4E-06
A_{20}	Z^2C	-2.3E-07	9.3E-07	-1.6E-07	-7.3E-07	-6.4E-07	-4.5E-04	-5.7E-07	-1.8E-07
$A_{2,-1}$	ZY	1.6E-08	3.2E-08	-7.6E-07	3.7E-06	-1.3E-07	3E-07	1.8E-04	9.7E-07
$A_{2,-2}$	XY	7.1E-09	-1.3E-08	1.6E-07	3.0E-06	-1.5E-07	3.3E-07	-3.1E-07	2.1E-04
	C	-1.0E-05	7.3E-06	-2.4E-05	3.4E-04	2.2E-04	-1.2E-06	2.0E-04	-2.7E-04

Table 2. The R^2 values of linear fits for respective shims. Numbers highlighted in green (diagonal) indicate almost perfect correlation with DAC settings. Numbers highlighted in light blue (off diagonal) indicate strong cross influences between coils with changing DAC settings. In other words, a given second order shim coil can produce undesired field components that project onto the entire spherical harmonic coefficient set.

Coefficient	Notation	Ra							
		X-Coil	Z-Coil	Y-Coil	X ² Y ² -Coil	XZ-Coil	Z ² C-Coil	ZY-Coil	XY-Coil
A_{11}	X	1.00E+00	7.27E-02	2.96E-01	9.96E-01	9.66E-01	9.94E-01	9.98E-01	9.95E-01
A_{10}	Z	3.69E-02	1.00E+00	3.78E-01	9.99E-01	9.74E-01	1.93E-01	7.98E-01	1.00E+00
$A_{1,-1}$	Y	2.82E-01	4.08E-01	1.00E+00	9.03E-01	9.98E-01	9.86E-01	9.88E-01	9.94E-01
A_{22}	$X^2 - Y^2$	2.23E-01	3.74E-01	4.17E-02	1.00E+00	1.01E-01	6.28E-01	1.31E-01	9.99E-01
A_{21}	ZX	7.99E-01	1.61E-01	5.03E-02	9.99E-01	9.99E-01	8.99E-01	6.25E-01	9.98E-01
A_{20}	Z^2C	2.47E-01	3.69E-01	9.86E-02	7.06E-01	9.57E-01	1.00E+00	9.83E-01	1.07E-01
$A_{2,-1}$	ZY	1.11E-02	5.25E-03	6.73E-01	9.94E-01	4.75E-01	8.72E-01	9.99E-01	9.20E-01
$A_{2,-2}$	XY	6.45E-03	1.32E-02	1.87E-01	9.99E-01	6.53E-01	8.63E-01	8.55E-01	1.00E+00
	C	8.91E-02	4.02E-02	4.19E-01	9.92E-01	9.90E-01	1.07E-06	9.83E-01	9.91E-01

second-order harmonics (*i.e.*, $x^2 - y^2$, xz , and zy) in addition to first-order harmonics. On the other hand, both **Table 1** & **Table 2** suggest that DAC changes in first-order shims are relatively independent and only influence the first three spherical harmonic calibration constants (e.g., A_{11} , A_{10} , A_{1-1}).

3.1. Active Shimming of a Phantom

Figure 1(A) and **Figure 1(B)** show B_0 field distribution in the phantom before and after active shimming. The histograms of magnetic field distributions (over the entire phantom), before and after active shimming, are shown in **Figure 2(A)** and **Figure 2(B)**. The full width at the half maximum (FWHM) value of the field distribution after active shimming is reduced by approximately 94.8% (**Figure 2(B)**). Note: **Figure 1(B)** and **Figure 2(B)** are similar to what can be achieved with the proposed shimming method, *i.e.*, using **Table 1**. These results show that our method improves B_0 homogeneity significantly within the phantom.

3.2. Comparison of FASTMAP and Corrected B_0 Field Maps Using the proposed Method in a Human Brain

B_0 maps following FASTMAP and active shimming methods are shown in **Figure 3**. Significant field inhomogeneity can be observed after FASTMAP shimming (**Figure 3(A)**). The introduction of first- and second-order field corrections improved B_0 homogeneity (**Figure 3(B)** and **Figure 3(C)**), although, the prefrontal cortex and regions near the nasal sinus still remained inhomogeneous. The large susceptibility variations made shimming these regions difficult, whenever the VOI includes the whole brain.

Figure 4 shows the FWHMs after respective shim procedures. With FASTMAP, the FWHM is about 127.1 Hz. This value was reduced to 91.9 Hz after optimal first- and second-order shimming which is a 28% improvement in the field homogeneity (**Figure 4(B)**). This value was further improved (by approximately 38%) after incorporating the corrections shown in Equation (5), (**Figure 4(C)**).

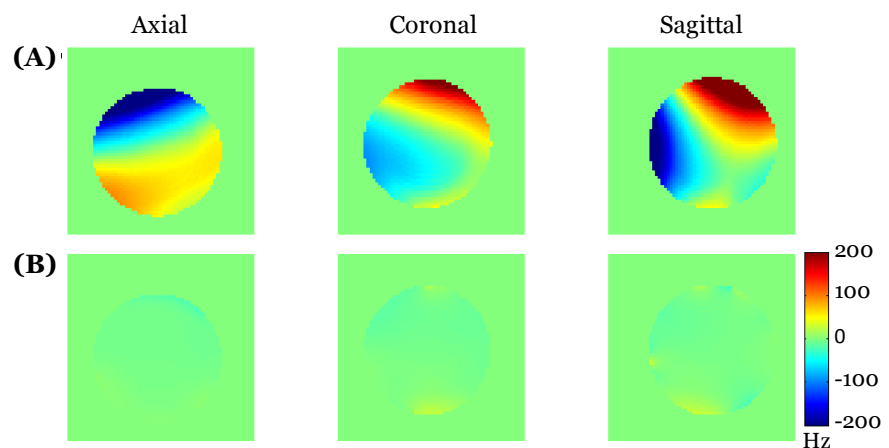


Figure 1. Comparison of B_0 magnetic field homogeneity within the phantom before (A) and after (B) active shimming. The calibration table is used to achieve the optimization of the field homogeneity.

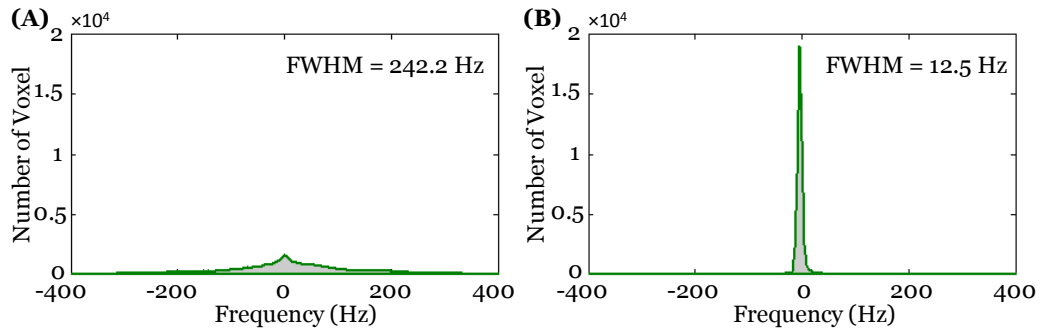


Figure 2. The histograms of the magnetic field variation of the phantom before (A) and after (B) active shimming. A narrower histogram indicates a highly uniform magnetic field over the entire phantom.

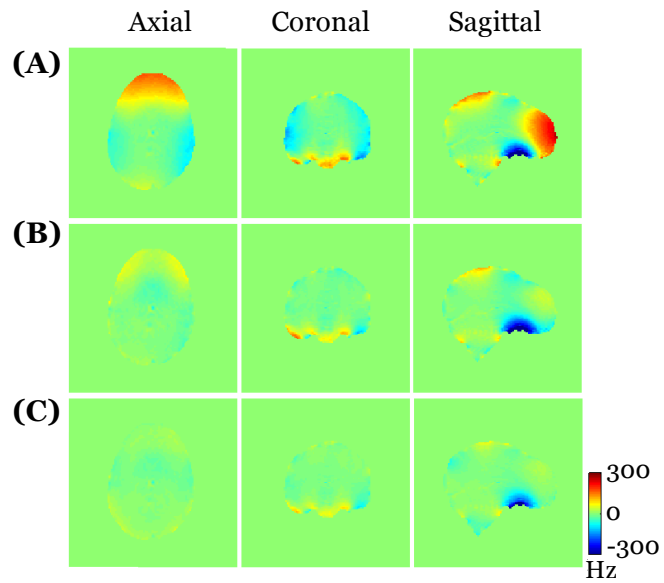


Figure 3. B_0 field maps of a subject’s brain at the center slice (A) after FASTMAP shimming and (B) after adjusting optimal first- and second-order corrections and (C) after incorporating adjustments given by Equation (5) to optimal first and second-order corrections.

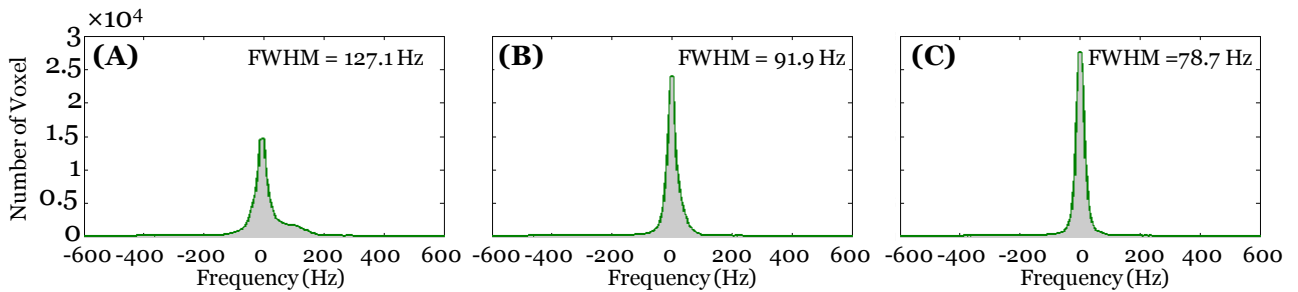


Figure 4. Histograms of the magnetic field variations in the brain corresponding to field maps shown in Figure 3. A narrower histogram indicates a more uniform magnetic field over the entire brain.

4. Discussion and Conclusion

Performance analyses of phantom results and *in vivo* results of a human brain showed that our proposed method can significantly outperform FASTMAP.

When field maps are derived using all data points within a VOI, B_0 homogeneity can be improved by countering the contributions, or effects, of higher-order shims on first-order shims. First order shims play significant roles in B_0 homogeneity within small VOIs. Accordingly, taking into account the contributions of higher order shims within small VOIs can be important for many MR spectroscopy applications. Specifically, our method highlights the advantage of using spherical harmonic expansion corrections for shimming spherical volumes.

Our method, however, could not improve the magnetic field homogeneity near regions of the nasal sinus to a satisfying degree: these regions are known for significant susceptibility variations. Future research, focusing on combining active and passive shimming, must be pursued in order to further improve field homogeneity in the frontal brain [27]. Combining these two shimming techniques could be very important for high field MR setups which inherently require higher second-order shim fields [8] [28] [29].

Magnetic field gradient pulses can produce eddy-currents in conductive brain regions [17] [30] [31], affecting the accuracy of field map calculations. These effects can be mitigated by fixing the relative timing of gradient pulses immediately preceding excitation pulses or acquisition windows during $\delta 1$ and $\delta 2$ (see **Figure S1** for details).

There may be instances where simultaneous shimming of arbitrary volumes (with differing levels of field uniformity) becomes necessary. For example: to establish a shim over a particular organ, with a tight B_0 range, while maintaining a coarser uniformity over the entire abdominal slice to prevent frequency-based fat-suppression techniques from failing. Thus, our method provides greater flexibility and can be advantageous for shimming arbitrary volumes over FASTMAP.

Here, we followed the method of projecting shim maps onto spherical harmonics: an *a priori* basis set to represent field maps. Due to some arguments suggesting that the use of spherical harmonics may be sub-optimal [22], Webb *et al.* (1991) used shim maps themselves as basis sets to produce highly uniform B_0 fields over large volumes [31] [32]. A performance analysis comparing our techniques with theirs should be the focus of future research.

Conflicts of Interest

The authors declare no conflicts of interest regarding the publication of this paper.

References

- [1] Gruetter, R. and Tkáč, I. (2000) Field Mapping without Reference Scan Using Asymmetric Echo-Planar Techniques. *Magnetic Resonance in Medicine*, **43**, 319-323. [https://doi.org/10.1002/\(SICI\)1522-2594\(200002\)43:2%3C319::AID-MRM22%3E3.0.CO;2-1](https://doi.org/10.1002/(SICI)1522-2594(200002)43:2%3C319::AID-MRM22%3E3.0.CO;2-1)
- [2] Sumanaweera, T.S., Glove, G.H., Binford, T.O. and Adler, J.R. (1993) MR Susceptibility Misregistration Correction. *IEEE Transactions on Medical Imaging*, **12**, 251-259. <https://doi.org/10.1109/42.232253>

- [3] Holz, D., Jensen, D., Proksa, R., Tochtrop, M. and Vollmann, W. (1988) Automatic Shimming for Localized Spectroscopy. *Medical Physics*, **15**, 898-903. <https://doi.org/10.1118/1.596173>
- [4] Doddrell, D.M., Galloway, G.J., Brewton, I.M. and Brooks, W.M. (1988) Nodal Inhomogeneity Mapping by Localized Excitation—The “NIMBLE” Shimming Technique for High-Resolution *in Vivo* NMR Spectroscopy. *Magnetic Resonance in Medicine*, **7**, 352-357. <https://doi.org/10.1002/mrm.1910070313>
- [5] Hoult, D. (1987) Shimming on Spatially Localized Signals. *Journal of Magnetic Resonance*, **73**, 174-177. [https://doi.org/10.1016/0022-2364\(87\)90238-1](https://doi.org/10.1016/0022-2364(87)90238-1)
- [6] Haacke, E.M., *et al.* (1999) *Magnetic Resonance Imaging: Physical Principles and Sequence Design*. Wiley-Liss, New York.
- [7] Wilson, J.L., Jenkinson, M. and Jezzard, P. (2002) Optimization of Static Field Homogeneity in Human Brain Using Diamagnetic Passive Shims. *Magnetic Resonance in Medicine*, **48**, 906-914. <https://doi.org/10.1002/mrm.10298>
- [8] Juchem, C., *et al.* (2006) Combined Passive and Active Shimming for *in Vivo* MR Spectroscopy at High Magnetic Fields. *Journal of Magnetic Resonance*, **183**, 278-289. <https://doi.org/10.1016/j.jmr.2006.09.002>
- [9] Cusack, R., *et al.* (2005) An Evaluation of the Use of Passive Shimming to Improve Frontal Sensitivity in fMRI. *NeuroImage*, **24**, 82-91. <https://doi.org/10.1016/j.neuroimage.2004.08.029>
- [10] Koch, K.M., *et al.* (2006) Sample-Specific Diamagnetic and Paramagnetic Passive Shimming. *Journal of Magnetic Resonance*, **182**, 66-74. <https://doi.org/10.1016/j.jmr.2006.06.013>
- [11] Klassen, L.M. and Menon, R.S. (2004) Robust Automated Shimming Technique Using Arbitrary Mapping Acquisition Parameters (RASTAMAP). *Magnetic Resonance in Medicine*, **51**, 881-887. <https://doi.org/10.1002/mrm.20094>
- [12] Jayatilake, M., Storrs, J. and Lee, J.-H. (2008) Comparison of FASTMAP and B0 Field Map Shimming for 4T MR. University of Cincinnati, Ohio.
- [13] Gruetter, R. (1993) Automatic, Localized *in Vivo* Adjustment of All First-And Second-Order shim coils. *Magnetic Resonance in Medicine*, **29**, 804-811. <https://doi.org/10.1002/mrm.1910290613>
- [14] Gruetter, R. and Boesch, C. (1992) Fast, Noniterative Shimming of Spatially Localized Signals. *In Vivo* Analysis of the Magnetic Field along Axes. *Journal of Magnetic Resonance*, **96**, 323-334. [https://doi.org/10.1016/0022-2364\(92\)90085-L](https://doi.org/10.1016/0022-2364(92)90085-L)
- [15] Miyasaka, N., Takahashi, K. and Hetherington, H.P. (2006) Fully automated Shim Mapping Method for Spectroscopic Imaging of the Mouse Brain at 9.4 T. *Magnetic Resonance in Medicine*, **55**, 198-202. <https://doi.org/10.1002/mrm.20731>
- [16] Hsu, J.J. and Glover, G.H. (2005) Mitigation of Susceptibility-Induced Signal Loss in Neuroimaging Using Localized Shim Coils. *Magnetic Resonance in Medicine*, **53**, 243-248. <https://doi.org/10.1002/mrm.20365>
- [17] Mackenzie, I.S., Robinson, E.M., Wells, A.N. and Wood, B. (1987) A Simple Field Map for Shimming. *Magnetic Resonance in Medicine*, **5**, 262-268. <https://doi.org/10.1002/mrm.1910050307>
- [18] Prammer, M.G., *et al.* (1988) A New Approach to Automatic Shimming. *Journal of Magnetic Resonance* (1969), **77**, 40-52. [https://doi.org/10.1016/0022-2364\(88\)90030-3](https://doi.org/10.1016/0022-2364(88)90030-3)
- [19] Wen, H. and Jaffer, F.A. (1995) An *in Vivo* Automated Shimming Method Taking into Account Shim Current Constraints. *Magnetic Resonance in Medicine*, **34**, 898-904.

- <https://doi.org/10.1002/mrm.1910340616>
- [20] Shen, J., Rothman, D.L., Hetherington, H.P. and Pan, J.W. (1999) Linear Projection Method for Automatic Slice Shimming. *Magnetic Resonance in Medicine*, **42**, 1082-1088. [https://doi.org/10.1002/\(SICI\)1522-2594\(199912\)42:6%3C1082::AID-MRM12%3E3.0.CO;2-G](https://doi.org/10.1002/(SICI)1522-2594(199912)42:6%3C1082::AID-MRM12%3E3.0.CO;2-G)
- [21] Chen, Z., *et al.* (2004) Measurement and Automatic Correction of High-Order B₀ Inhomogeneity in the Rat Brain at 11.7 Tesla. *Magnetic Resonance Imaging*, **22**, 835-842. <https://doi.org/10.1016/j.mri.2004.01.062>
- [22] Roméo, F. and Hoult, D.I. (1984) Magnet Field Profiling: Analysis and Correcting Coil Design. *Magnetic Resonance in Medicine*, **1**, 44-65. <https://doi.org/10.1002/mrm.1910010107>
- [23] Shen, J., Rycyna, R.E. and Rothman, D.L. (1997) Improvements on an *in Vivo* Automatic Shimming Method (FASTERMAP). *Magnetic resonance in Medicine*, **38**, 834-839. <https://doi.org/10.1002/mrm.1910380521>
- [24] Glover, G. and Schneider, E. (1991) Three-Point Dixon Technique for True Water/Fat Decomposition with B₀ Inhomogeneity Correction. *Magnetic Resonance in Medicine*, **18**, 371-383. <https://doi.org/10.1002/mrm.1910180211>
- [25] Reynaud, O., *et al.* (2015) Fast Low-Specific Absorption Rate B₀-Mapping along Projections at High Field Using Two-Dimensional Radiofrequency Pulses. *Magnetic Resonance in Medicine*, **73**, 901-908. <https://doi.org/10.1002/mrm.25217>
- [26] Zhang, Y., Li, S. and Shen, J. (2009) Automatic High-Order Shimming Using Parallel Columns Mapping (PACMAP). *Magnetic Resonance in Medicine*, **62**, 1073-1079. <https://doi.org/10.1002/mrm.22077>
- [27] Jayatilake, M., *et al.* (2011) Construction and Optimization of Local 3rd Order Passive Shim System for Human Brain Imaging at 4T MRI. *Proceedings of the International Society for Magnetic Resonance in Medicine*, **19**, 3785.
- [28] Jackson, J.D. (1999) Classical Electrodynamics. 3rd Edition, Wiley, Hoboken.
- [29] Arfken, G.B. and Weber, H.J. (1999) Mathematical Methods for Physicists. 4th Edition, Academic Press, Cambridge.
- [30] Kim, D.H., Adalsteinsson, E., Glover, G.H. and Spielman, D.M. (2002) Regularized Higher-Order *in Vivo* Shimming. *Magnetic Resonance in Medicine*, **48**, 715-722. <https://doi.org/10.1002/mrm.10267>
- [31] Webb, P. and Macovski, A. (1991) Rapid, Fully Automatic, Arbitrary-Volume *in Vivo* Shimming. *Magnetic Resonance in Medicine*, **20**, 113-122. <https://doi.org/10.1002/mrm.1910200112>
- [32] Kanayamay, S., Kuhara, S. and Satoh, K. (1996) *In Vivo* Rapid Magnetic Field Measurement and Shimming Using Single Scan Differential Phase Mapping. *Magnetic Resonance in Medicine*, **36**, 637-642. <https://doi.org/10.1002/mrm.1910360421>

Supplementary Materials

Inhomogeneous magnetic fields in the MRI scanner can be corrected by adjusting shim coils to produce additional magnetic fields. These shim coils generate unique magnetic field distributions which are modelled using orthogonal spherical harmonic functions [5] [14] [15] [16] [17] [19].

Below, we present the theory and methods to: 1) numerically estimate inhomogeneous magnetic fields by varying shim settings; 2) derive calibration tables, and (3) determine appropriate shim currents for the first and second-order shim coils.

S.1. Modeling the B_0 Static Magnetic Field

Assuming a current density of zero ($\bar{J} = 0$), the static inhomogeneous magnetic field ΔB_0 in a region of interest is given by Laplace's equation (S1).

$$\nabla^2 (\Delta B_0) = 0 \tag{S1}$$

The solution to this equation ΔB_0 can be expressed as a sum of spherical harmonics [14] [20] [29].

$$\Delta B_0 (r, \theta, \phi) = \sum_{n=0}^{\infty} \sum_{m=0}^n A_{nm} r^n \cdot P_{n,m} (\cos \theta) \cdot e^{jm\phi} \tag{S2}$$

Here, r, θ and ϕ are the spherical coordinates. n and m are integers satisfying the conditions $n \geq m \geq 0$; n is the order and m is the degree of a given spherical harmonic. A_{nm} are the coefficients of spherical harmonic functions. The $P_{n,m} (\cos \theta)$ is Ferrer's associated Legendre polynomial [26], and ΔB_0 can be expressed in terms of Cartesian coordinates using **Table S1**.

$$\begin{aligned} \Delta B_0 (x, y, z) = & c + \alpha_{11}x + \alpha_{10}z + \alpha_{1-1}y + \alpha_{22}(x^2 - y^2) + \alpha_{21}zx \\ & + \alpha_{20}(z^2 - 1/2(x^2 + y^2)) + \alpha_{2-1}zy + \alpha_{2-2}xy + \dots \end{aligned} \tag{S3}$$

Table S1. Converting first, and second-order, spatially-dependent, spherical harmonic functions to Cartesian coordinates.

n	m	Short-hand notation	Coefficient (α_{nm})	Spatial dependence function	
				Spherical	Cartesian
1	1	X	α_{11}	$r \cdot \sin \theta \cdot \cos \phi$	x
1	0	Z	α_{10}	$r \cdot \cos \theta$	z
1	-1	Y	α_{1-1}	$r \cdot \sin \theta \cdot \sin \phi$	y
2	2	$X^2 - Y^2$	α_{22}	$r^2 \cdot \sin^2 \theta \cdot \cos 2\phi$	$x^2 - y^2$
2	1	ZX	α_{21}	$r^2 \cdot \sin \theta \cdot \cos \theta \cdot \cos \phi$	xz
2	0	ZZC	α_{20}	$r^2 \cdot (3 \cos^2 \theta - 1) / 2$	$z^2 - (x^2 + y^2) / 2$
2	-1	ZY	α_{2-1}	$r^2 \cdot \sin \theta \cdot \cos \theta \cdot \sin \phi$	yz
2	-2	XY	α_{2-2}	$r^2 \cdot \sin^2 \theta \cdot \cos \phi \cdot \sin \phi$	xz

S.2. Experimentally Determining $\Delta B_0(x, y, z)$

We performed a phantom study using the pulse sequence shown in **Figure S1** to compute the B_0 field maps. $\Delta B_0(x, y, z)$ was computed by comparing two phase images with different echo times.

At each voxel, the relationship between $\Delta B_0(x, y, z)$, phase evolution $\Delta\phi(x, y, z)$, and echo time (ΔTE) is given by Equation (S4):

$$\Delta B_0(x, y, z) = \frac{\Delta\phi(x, y, z)}{\gamma \cdot \Delta TE}. \tag{S4}$$

Here γ is the gyromagnetic ratio in radian/s/T for proton $\gamma(^1\text{H}) = 2.675 \times 10^8 \text{ rad} \cdot \text{s}^{-1} \cdot \text{T}^{-1}$. Since the phase can only have magnitudes between $-2\pi < \phi < 2\pi$, phase unwrapping must be performed on an as needed basis. At each voxel, the distribution of the precessional frequency $f(x, y, z)$ is related to $\Delta B_0(x, y, z)$ by Equation (S5):

$$f(x, z, y) = \frac{\gamma \cdot \Delta B_0(x, y, z)}{2\pi}. \tag{S5}$$

These $f(x, y, z)$ maps were computed for DAC values: (A) $-15,000$, (B) $-10,000$, (C) -5000 , (D) 0 , (E) 5000 , (F) $10,000$, and (G) $15,000$.

S.3. Phantom Study

This procedure was repeated on a water phantom to compute frequency distribution maps. **Figure S2** and **Figure S3** show $f(x, y, z)$ maps for the water phantom, for all 8 shim coils.

S.3.1. Computing Calibration Tables

By combining Equation (S3) and Equation (S5) we obtain the following expression

$$f(x, y, z) = c' + \eta_{11}x + \eta_{10}z + \eta_{1-1}y + \dots + \eta_{22}(x^2 - y^2) + \eta_{21}zx + \eta_{20}(z^2 - 1/2(x^2 + y^2)) + \eta_{2-1}zy + \eta_{2-2}xy + \dots \tag{S6}$$

Here, c' and η represent the 0th and higher-order coefficients of spherical harmonics. The matrix representation of $f(x, y, z)$ is given by:

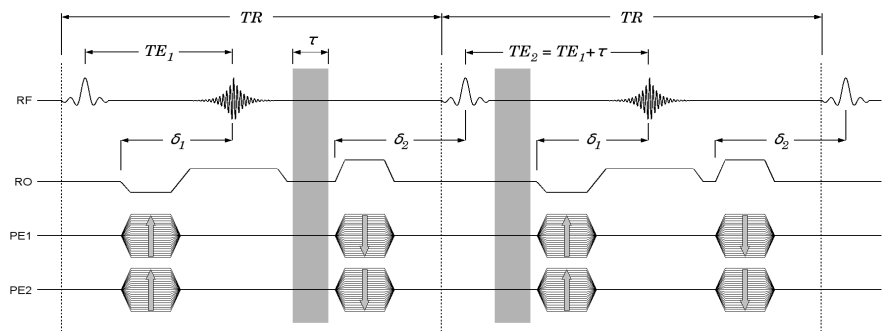


Figure S1. The modified 3D-gradient-echo pulse sequence.

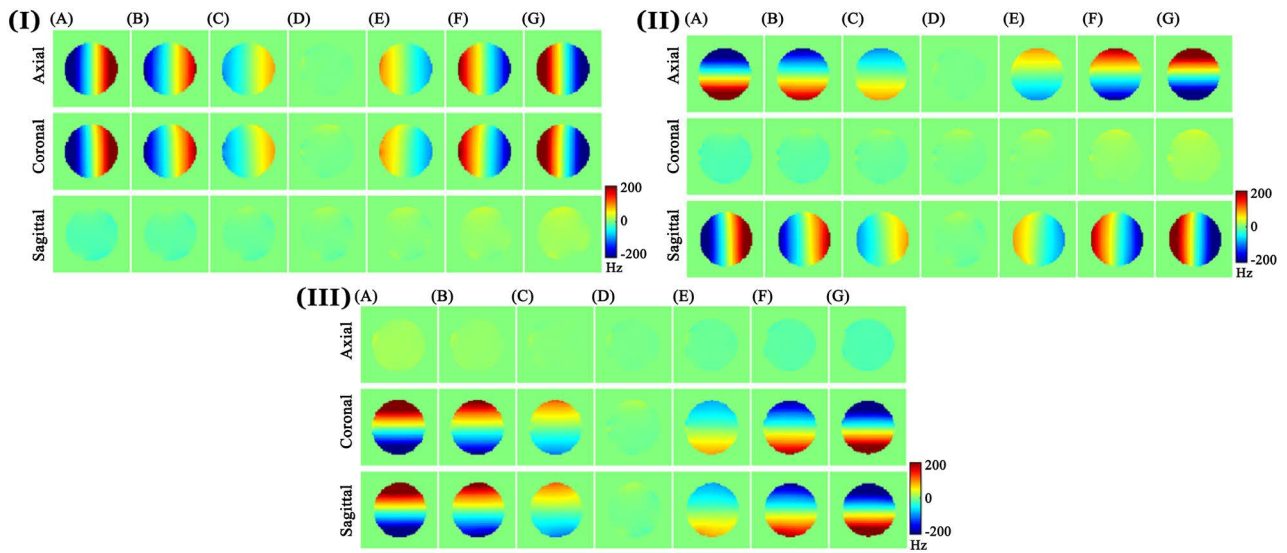


Figure S2. $\Delta B_0(x, y, z)$ maps for the first order shim coils: (I) X, (II) Y and (III) Z. These maps correspond to DAC settings of $-15,000$ to $15,000$, moving by increments of $+5000$ for each step.

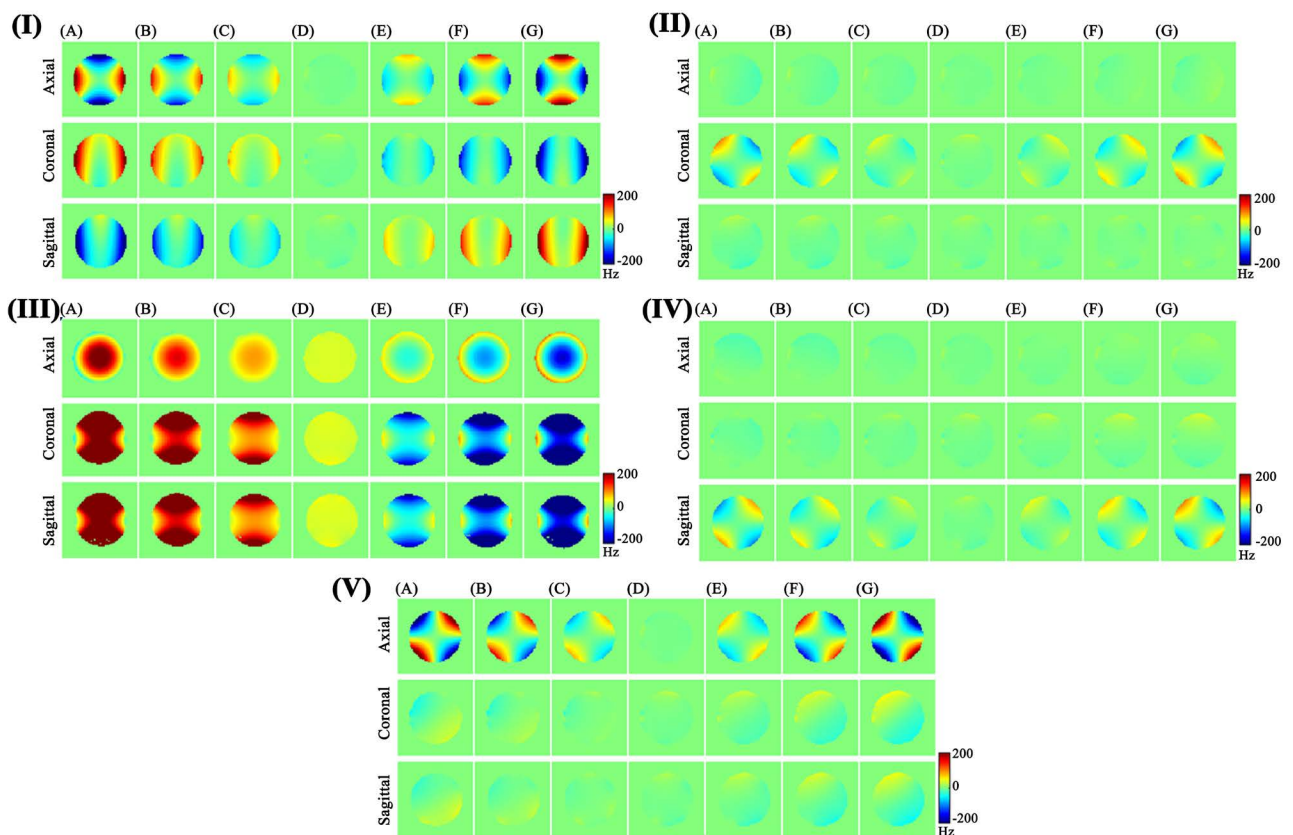


Figure S3. $\Delta B_0(x, y, z)$ field maps for the second-order shim coils: (I) $X^2 - Y^2$, (II) XZ , (III) Z^2C , (IV) YZ and (V) XY . These maps correspond to DAC settings of $-15,000$ to $15,000$, moving by increments of $+5000$ for each step.

$$f(x, y, z) = \sum_{n=0}^{\infty} \sum_{m=0}^n F_{n,m}(x_i, y_j, z_k) \cdot \eta_{nm} \quad (S7)$$

where η_{nm} are the coefficients of spherical harmonics. Using the linear least-squares method, the optimized spherical harmonic coefficients of the first and second-order shim coils can be estimated. The frequency distributions of all shim coils (at each DAC step) can be projected onto spherical harmonics by using Equation (S7). We assume that the $\eta_{nm,g,l}$ of each shim coil is linearly varying with the DAC values, *i.e.*,

$$\eta_{nm,g,l} = C_{nm,g} \cdot DAC_{l,g}. \tag{S9}$$

Here $C_{nm,g}$ is the calibration constant for each spherical harmonic. These $C_{nm,g}$ values can be estimated using the following expression:

$$C_{nm,g} = \left(\left(DAC_{l,g}^T \cdot DAC_{l,g} \right)^{-1} \cdot DAC_{l,g} \cdot \eta_{nm,g,l}^T \right)^T. \tag{S10}$$

The values for all 8 shim coils are computed using tables and **Figures S4-S6** shown below. Finally, the spherical harmonic calibration constants are computed by the gradients between spherical harmonic coefficients and the DAC values of each coil. This can be used to update the DAC settings.

(A)

Coefficient	Notation	DAC							Slope ($C_{nm,g}$)	R^2
		-15000	-10000	-5000	0	5000	10000	15000		
$A_{1,1}$	X	3.4E+01	2.3E+01	1.1E+01	-1.5E-01	-1.2E+01	-2.3E+01	-3.4E+01	-2.3E-03	1.0E+00
$A_{1,0}$	Z	-4.9E-01	-4.9E-01	-5.5E-01	-5.8E-01	-5.3E-01	-5.3E-01	-5.0E-01	-6.2E-07	3.7E-02
$A_{1,-1}$	Y	-8.4E-02	-7.9E-02	-1.4E-01	-1.3E-01	-1.3E-01	-1.1E-01	-1.2E-01	-1.1E-06	2.8E-01
$A_{2,2}$	X2 - Y2	-7.4E-03	-6.9E-03	1.1E-02	1.7E-03	1.7E-02	-2.2E-04	4.5E-03	3.9E-07	2.2E-01
$A_{2,1}$	ZX	1.6E-03	5.2E-04	-9.6E-03	-8.9E-03	-4.6E-03	-2.0E-02	-2.4E-02	-8.0E-07	8.0E-01
$A_{2,0}$	Z2C	3.9E-02	4.0E-02	3.3E-02	4.4E-02	2.9E-02	3.6E-02	3.3E-02	-2.3E-07	2.5E-01
$A_{2,-1}$	ZY	1.4E-02	1.2E-02	1.2E-02	1.6E-02	1.2E-02	1.6E-02	1.2E-02	1.6E-08	1.1E-02
$A_{2,-2}$	XY	7.1E-05	1.9E-03	2.5E-03	1.2E-03	-1.6E-04	1.2E-03	1.7E-03	7.1E-09	6.5E-03
	C	-2.0E+00	-2.0E+00	-2.0E+00	-3.0E+00	-2.2E+00	-2.2E+00	-2.2E+00	-1.0E-05	8.9E-02

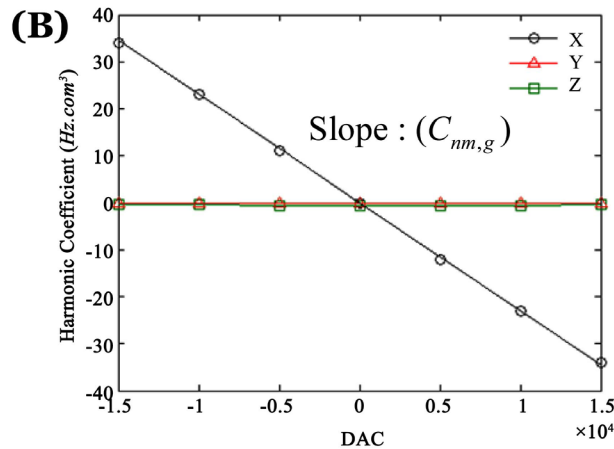


Figure S4. (A) The first- and second-order spherical harmonic coefficients for the X coil ($\text{Hz}\cdot\text{cm}^{-1}$ and $\text{Hz}\cdot\text{cm}^{-2}$) at DAC values of $-15,000$, $-10,000$, $-5,000$, 0 , $5,000$, $10,000$, and $15,000$. For each DAC value, $\Delta B_0(x, y, z)$ maps were computed and spherical harmonic coefficients were estimated using the least-squares technique. (B) Using linear regression, the spherical harmonic calibration constant ($C_{nm,g}$) for the X coil (highlighted in orange) is estimated as the gradient (slope) between spherical harmonic coefficients (yellow) and the DAC values. The linear fit of this regression (R^2) is also computed. The procedure is explained in the graph above. The same procedure was repeated for other shims.

The calibration constants and their corresponding R^2 are obtained from **Figure S4** & **Figure S5** and used in **Table 1** and **Table 2**.

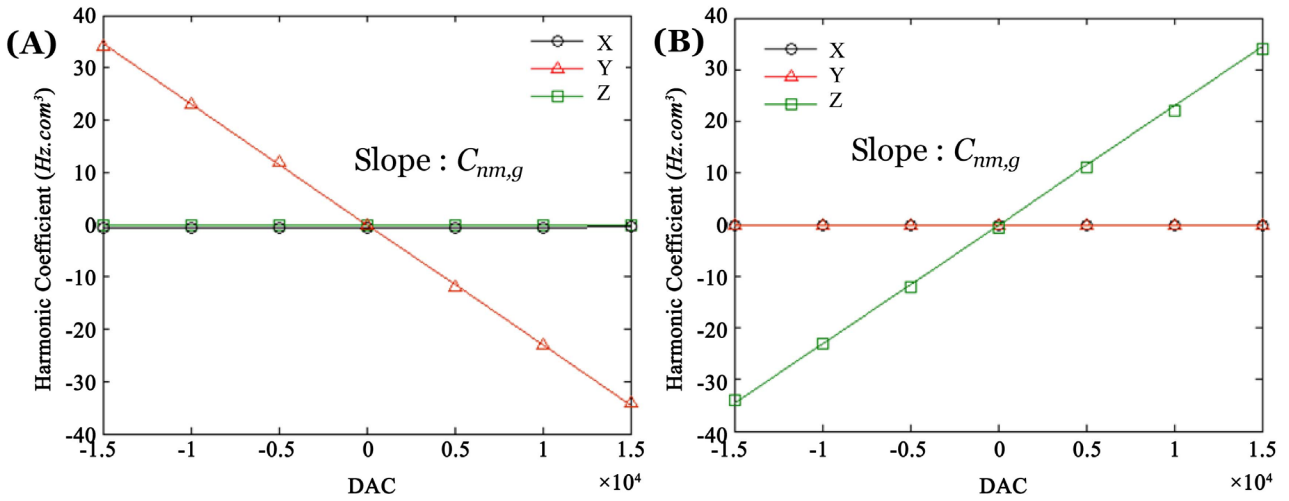
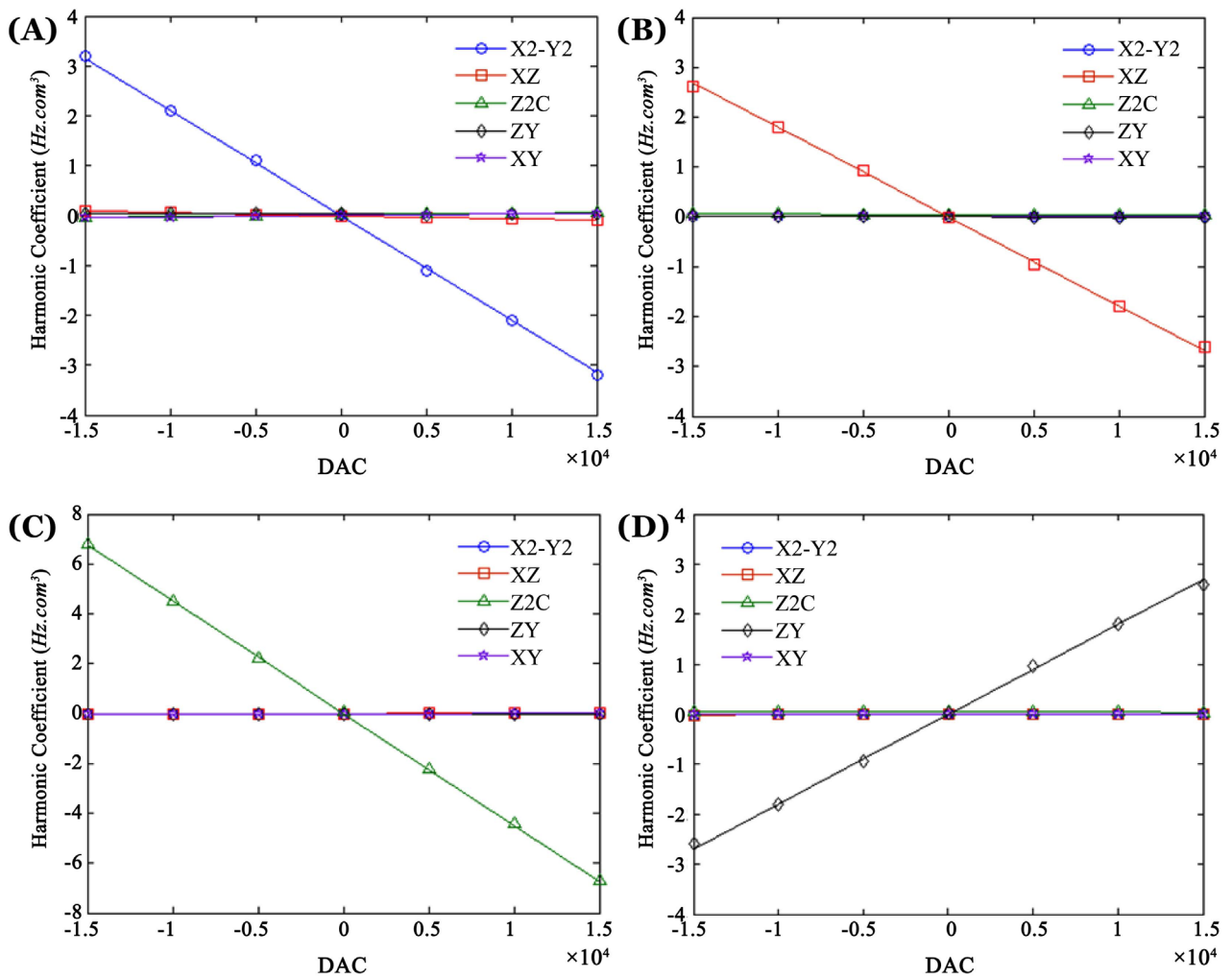


Figure S5. The gradient [slope: spherical harmonic calibration constant ($C_{nm,g}$)] estimates for Y and Z coils. The linear fits of regression (R^2) are computed using figures similar to **Figure S4**. The same procedure described in **Figure S4** was followed.



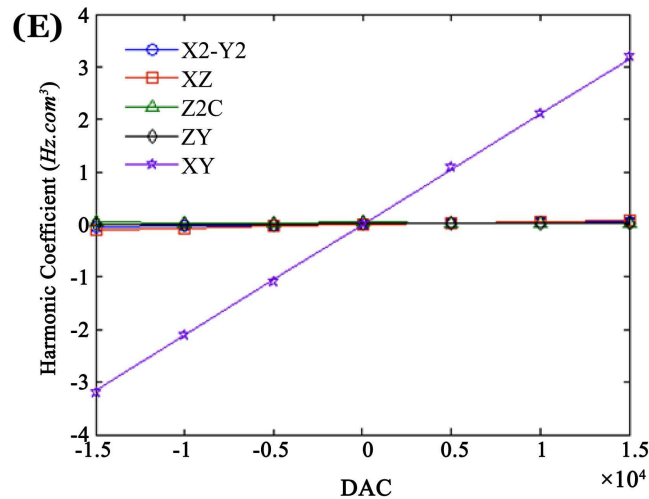


Figure S6. The gradient [slope: spherical harmonic calibration constant ($C_{nm,g}$)] are estimates for $X^2 - Y^2$, XZ , Z^2C , ZY and XY coils. The linear fits of regression (R^2) are computed using figures similar to **Figure S4**. The same procedure described in **Figure S4** was followed.

Abbreviation

B_0 : Static main magnetic field

FASTMAP: Fast automatic shimming technique, by mapping along projections

DAC: Digital to Analog Converter

n : Order of a spherical harmonic

m : Degree of a spherical harmonic

η_{nm} : Coefficients of spherical harmonics

$P_{n,m}(x, y, z)$: Cartesian spherical harmonic spatial dependence function

$C_{nm,g}$: Calibration constant.

R^2 : Linear fit

\bar{J} : Current density

ΔB_0 : Static inhomogeneous magnetic field

$P_{n,m}(\cos\theta)$: Ferrer's associated Legendre polynomial

$\Delta\phi(x, y, z)$: Phase evolution

ΔTE : Echo time

γ : Gyromagnetic ratio in radian/s/T.

$f(x, y, z)$: Precessional frequency distribution at each voxel

c' : 0th coefficients of spherical harmonic

η_{nm} : Coefficients of spherical harmonics.

$C_{nm,g}$: Calibration constant for each spherical harmonic.

VOI: Volume of Interest